












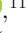


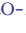
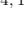



















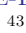















The DESI DR1 Peculiar Velocity Survey: The Tully-Fisher Distance Catalog

K. DOUGLASS ¹, S. BENZVI ¹, A. G. KIM ², S. MOORE ¹, A. CARR ³, J. LARGETT ¹, N. RAVI ¹, J. AGUILAR,²
S. AHLEN ⁴, A. J. AMSELLEM ⁵, J. BAUTISTA,⁶ D. BIANCHI ^{7,8}, C. BLAKE ⁹, D. BROOKS,¹⁰ T. CLAYBAUGH,²
A. CUCEU ², A. DE LA MACORRA ¹¹, R. DEMINA ¹, P. DOEL,¹⁰ S. FERRARO ^{2,12}, A. FONT-RIBERA ¹³,
J. E. FORERO-ROMERO ^{14,15}, E. GAZTAÑAGA ^{16,17,18}, S. GONTCHO A GONTCHO ^{2,19}, G. GUTIERREZ,²⁰ J. GUY ²,
H. K. HERRERA-ALCANTAR ^{21,22}, K. HONSCHIED ^{23,24,25}, C. HOWLETT ²⁶, D. HUTERER ^{27,28}, M. ISHAK ²⁹,
R. JOYCE ³⁰, A. KREMIN ², O. LAHAV,¹⁰ C. LAMMAN ²⁵, M. LANDRIAU ², L. LE GUILLOU ³¹,
A. LEAUTHAUD ^{32,33}, M. E. LEVI ², M. MANERA ^{34,13}, P. MARTINI ^{23,35,25}, A. MEISNER ³⁰, R. MIQUEL,^{36,13}
J. MOUSTAKAS ³⁷, A. MUÑOZ-GUTIÉRREZ,¹¹ S. NADATHUR ¹⁷, N. PALANQUE-DELABROUILLE ^{22,2}, A. PALMESE,⁵
W. J. PERCIVAL ^{38,39,40}, C. POPPETT,^{2,41,12} F. PRADA ⁴², I. PÉREZ-RÀFOLS ⁴³, F. QIN ⁶, C. ROSS ²⁶, G. ROSSI,⁴⁴
K. SAID ²⁶, E. SANCHEZ ⁴⁵, D. SCHLEGEL,² M. SCHUBNELL,²⁷ H. SEO ⁴⁶, J. SILBER ², D. SPRAYBERRY,³⁰
G. TARLÉ ²⁸, R. J. TURNER ⁹, B. A. WEAVER,³⁰ R. ZHOU ² AND H. ZOU ⁴⁷

¹Department of Physics & Astronomy, University of Rochester, 206 Bausch and Lomb Hall, P.O. Box 270171, Rochester, NY 14627-0171, USA

²Lawrence Berkeley National Laboratory, 1 Cyclotron Road, Berkeley, CA 94720, USA

³Korea Astronomy and Space Science Institute, 776, Daedeokdae-ro, Yuseong-gu, Daejeon 34055, Republic of Korea

⁴Department of Physics, Boston University, 590 Commonwealth Avenue, Boston, MA 02215 USA

⁵Department of Physics, Carnegie Mellon University, 5000 Forbes Avenue, Pittsburgh, PA 15213, USA

⁶Aix Marseille Univ, CNRS/IN2P3, CPPM, Marseille, France

⁷Dipartimento di Fisica “Aldo Pontremoli”, Università degli Studi di Milano, Via Celoria 16, I-20133 Milano, Italy

⁸INAF-Osservatorio Astronomico di Brera, Via Brera 28, 20122 Milano, Italy

⁹Centre for Astrophysics & Supercomputing, Swinburne University of Technology, P.O. Box 218, Hawthorn, VIC 3122, Australia

¹⁰Department of Physics & Astronomy, University College London, Gower Street, London, WC1E 6BT, UK

¹¹Instituto de Física, Universidad Nacional Autónoma de México, Circuito de la Investigación Científica, Ciudad Universitaria, Cd. de México C. P. 04510, México

¹²University of California, Berkeley, 110 Sproul Hall #5800 Berkeley, CA 94720, USA

¹³Institut de Física d’Altes Energies (IFAE), The Barcelona Institute of Science and Technology, Edifici Cn, Campus UAB, 08193, Bellaterra (Barcelona), Spain

¹⁴Departamento de Física, Universidad de los Andes, Cra. 1 No. 18A-10, Edificio Ip, CP 111711, Bogotá, Colombia

¹⁵Observatorio Astronómico, Universidad de los Andes, Cra. 1 No. 18A-10, Edificio H, CP 111711 Bogotá, Colombia

¹⁶Institut d’Estudis Espacials de Catalunya (IEEC), c/ Esteve Terradas 1, Edifici RDIT, Campus PMT-UPC, 08860 Castelldefels, Spain

¹⁷Institute of Cosmology and Gravitation, University of Portsmouth, Dennis Sciama Building, Portsmouth, PO1 3FX, UK

¹⁸Institute of Space Sciences, ICE-CSIC, Campus UAB, Carrer de Can Magrans s/n, 08913 Bellaterra, Barcelona, Spain

¹⁹University of Virginia, Department of Astronomy, Charlottesville, VA 22904, USA

²⁰Fermi National Accelerator Laboratory, PO Box 500, Batavia, IL 60510, USA

²¹Institut d’Astrophysique de Paris. 98 bis boulevard Arago. 75014 Paris, France

²²IRFU, CEA, Université Paris-Saclay, F-91191 Gif-sur-Yvette, France

²³Center for Cosmology and AstroParticle Physics, The Ohio State University, 191 West Woodruff Avenue, Columbus, OH 43210, USA

²⁴Department of Physics, The Ohio State University, 191 West Woodruff Avenue, Columbus, OH 43210, USA

²⁵The Ohio State University, Columbus, 43210 OH, USA

²⁶School of Mathematics and Physics, University of Queensland, Brisbane, QLD 4072, Australia

²⁷Department of Physics, University of Michigan, 450 Church Street, Ann Arbor, MI 48109, USA

²⁸University of Michigan, 500 S. State Street, Ann Arbor, MI 48109, USA

²⁹Department of Physics, The University of Texas at Dallas, 800 W. Campbell Rd., Richardson, TX 75080, USA

³⁰NSF NOIRLab, 950 N. Cherry Ave., Tucson, AZ 85719, USA

³¹Sorbonne Université, CNRS/IN2P3, Laboratoire de Physique Nucléaire et de Hautes Energies (LPNHE), FR-75005 Paris, France

³²Department of Astronomy and Astrophysics, UCO/Lick Observatory, University of California, 1156 High Street, Santa Cruz, CA 95064, USA

³³Department of Astronomy and Astrophysics, University of California, Santa Cruz, 1156 High Street, Santa Cruz, CA 95065, USA

³⁴*Departament de Física, Serra Hünter, Universitat Autònoma de Barcelona, 08193 Bellaterra (Barcelona), Spain*

³⁵*Department of Astronomy, The Ohio State University, 4055 McPherson Laboratory, 140 W 18th Avenue, Columbus, OH 43210, USA*

³⁶*Institució Catalana de Recerca i Estudis Avançats, Passeig de Lluís Companys, 23, 08010 Barcelona, Spain*

³⁷*Department of Physics and Astronomy, Siena University, 515 Loudon Road, Loudonville, NY 12211, USA*

³⁸*Department of Physics and Astronomy, University of Waterloo, 200 University Ave W, Waterloo, ON N2L 3G1, Canada*

³⁹*Perimeter Institute for Theoretical Physics, 31 Caroline St. North, Waterloo, ON N2L 2Y5, Canada*

⁴⁰*Waterloo Centre for Astrophysics, University of Waterloo, 200 University Ave W, Waterloo, ON N2L 3G1, Canada*

⁴¹*Space Sciences Laboratory, University of California, Berkeley, 7 Gauss Way, Berkeley, CA 94720, USA*

⁴²*Instituto de Astrofísica de Andalucía (CSIC), Glorieta de la Astronomía, s/n, E-18008 Granada, Spain*

⁴³*Departament de Física, EEBE, Universitat Politècnica de Catalunya, c/Eduard Maristany 10, 08930 Barcelona, Spain*

⁴⁴*Department of Physics and Astronomy, Sejong University, 209 Neungdong-ro, Gwangjin-gu, Seoul 05006, Republic of Korea*

⁴⁵*CIEMAT, Avenida Complutense 40, E-28040 Madrid, Spain*

⁴⁶*Department of Physics & Astronomy, Ohio University, 139 University Terrace, Athens, OH 45701, USA*

⁴⁷*National Astronomical Observatories, Chinese Academy of Sciences, A20 Datun Road, Chaoyang District, Beijing, 100101, P. R. China*

ABSTRACT

We calibrate the Tully-Fisher relation (TFR) using observations of spiral galaxies taken during the first year (DR1) of the DESI galaxy redshift survey. The rotational velocities of 10,262 galaxies are measured at $0.4R_{26}$ by comparing the redshifts at $0.4R_{26}$ with those at the galaxy centers of spatially-resolved galaxies targeted as part of the DESI Peculiar Velocity Survey. The DESI DR1 TFR slope is calibrated by separating the spiral galaxies into redshift bins of width $\Delta z = 0.005$ from $0.03 < z < 0.1$ and jointly fitting the TFR across all bins. We find a slope of -7.22 ± 0.01 AB mag in the r -band for the TFR, with an intrinsic scatter of 0.466 ± 0.001 AB mag. We present a catalog of the distances and peculiar velocities to these 10,262 galaxies using our calibrated TFR. For cosmological analyses, we also present a clustering catalog and associated random catalogs using a subset of 6807 of the DESI DR1 TF galaxies.

1. INTRODUCTION

Measuring distances to objects in the universe is a persistent challenge, but one that is necessary to tackle to progress the study of most areas of astrophysics and cosmology. Many methods for measuring distances to different types of objects have been developed, the most universal of which is Hubble’s Law (E. Hubble 1929) for extragalactic objects. While Hubble’s Law was almost immediately recognized as the ultimate distance indicator due to the ease with which one can measure an object’s redshift, its distances are plagued at low redshifts due to galaxies’ peculiar motions contributing to the observed redshift.

The interaction of the galaxy with its local gravitational potential due to the matter over- or under-densities produces the peculiar velocity (PV) of the galaxy (T. M. Davis & M. I. Scrimgeour 2014). The cosmological redshift of a galaxy, z_{cosmo} , and that due to its peculiar motion, z_{pec} , relate to the observed redshift, z_{obs} , as (E. R. Harrison 1974):

$$1 + z_{\text{obs}} = (1 + z_{\text{cosmo}})(1 + z_{\text{pec}}). \quad (1)$$

Disentangling a galaxy’s PV from its cosmological redshift requires a redshift-independent distance metric, often in the form of an empirically-calibrated distance indicator that relates a distance-independent quantity of

the galaxy with a distance-dependent property. Popular redshift-independent distance indicators include Type Ia supernovae (M. M. Phillips 1993), Surface Brightness Fluctuations (J. Tonry & D. P. Schneider 1988), the Fundamental Plane relation (FP; S. Djorgovski & M. Davis 1987; A. Dressler et al. 1987), and the Tully-Fisher relation (TFR; R. B. Tully & J. R. Fisher 1977).

The TFR relates the rotational velocity and luminosity of a galaxy. This relation thus applies to spiral galaxies: rotationally-supported systems where rotational velocity and luminosity are intrinsically related. While the physical origins of the TFR are not fully understood, a reasonable model for their behavior results from Newtonian dynamics. Assuming that the mass distribution of a galaxy is spherically symmetric, the centripetal acceleration in an object in circular orbit at radius r is equal to its gravitational acceleration from the interior mass of the sphere:

$$V_{\text{rot}}^2 \propto \frac{M(r)}{r}. \quad (2)$$

In the case of a constant mean surface brightness and mass-to-light ratio for spiral galaxies, this relation becomes

$$L \propto V_{\text{rot}}^4. \quad (3)$$

Many studies have found power-law exponents deviating from 4 both empirically (e.g., A. Sandage & G. A. Tam-

mann 1976; D. Burstein 1982; L. Bottinelli et al. 1983; M. J. Pierce & R. B. Tully 1988), and observationally (e.g., A. A. Ponomareva et al. 2017; E. Kourkchi et al. 2020a; K. Douglass et al. 2025). These deviations are often attributed to flaws in the assumption of a uniform mass-to-light ratio (J. Mould 2020).

In Tully-Fisher analyses, it is common to determine the rotational velocity of a galaxy based on the width of spectral lines such as the 21 cm H I line profile or the H α emission line. The H I profile allows for perhaps the most direct measurement of the maximum rotational velocity of a galaxy when there is sufficient neutral hydrogen present for its detection. The H α emission line is the most prominent in galaxy spectra at visible wavelengths, so it is the primary choice as a tracer of the rotational velocity of a spiral galaxy in the visible. It is more difficult to extract the maximum rotational velocity of a galaxy using H α emission lines, as measurements must be made at sufficiently large radii from the galaxy center to measure a flat rotation curve, a region where the H α surface brightness decreases rapidly and may be weak (Y. Sofue & V. Rubin 2001). This may result in a systematic underestimation of the maximum rotational velocity.

Once determined, the rotational velocity of a galaxy allows the luminosity, or absolute magnitude, to be estimated. The distance modulus is then determined by comparing this with the apparent magnitude of the galaxy. Previous TF distance catalogs produced include K. L. Masters et al. (2006), which used a mixture of H I line widths and optical rotation curves to measure the distance to ~ 5000 galaxies, and CosmicFlows (R. B. Tully & H. M. Courtois 2012; E. Kourkchi et al. 2020b), which relied on H I line widths to measure the distance to $\sim 10,000$ galaxies.

In this work, we expand on the TFR analysis performed on the DESI Early Data Release described in K. Douglass et al. (2025). We present a catalog of 10,262 PV measurements obtained with the TFR using the publicly available DESI Data Release 1 (DR1), representing $\sim 20\%$ of the data expected to be included in the final DESI data release. Alongside this, we present a clustering catalog, and associated random catalogs, using a subset of 6807 of these galaxies that are used in combination with the DESI DR1 Fundamental Plane sample (C. Ross et al. in prep.) and DESI DR1 mock PV catalogs (J. Bautista et al. in prep.) in the accompanying cosmological analyses of R. Turner et al. (in prep.); F. Qin et al. (in prep.); Y. Lai et al. (in prep.), and A. Carr et al. (in prep.). The TF catalog presented here is comparable in size to the TF catalog using H I line widths produced by Cosmicflows-4 (CF4; E. Kourkchi

et al. 2020b), currently the largest catalog of distances determined by the TFR. It covers a much smaller area of the sky (3580 sq. deg. relative to CF4’s almost full-sky coverage), but it more than doubles the redshift range ($z \lesssim 0.1$ relative to CF4’s $z < 0.05$) due to the use of the H α emission line instead of H I.

The layout of this paper is as follows. We first describe the DESI instrument, the DESI Peculiar Velocity Survey, and the DESI Data Release 1 (DR1) in Section 2. A description of our Tully-Fisher measurements, our quality selection criteria, and our estimated systematic uncertainties follow in Section 3. Section 4 discusses the calibration of the slope of the Tully-Fisher relation using data from DESI DR1. The measured Tully-Fisher relation for 10,262 galaxies in the DESI DR1 is presented in Section 5. We compare our results to previously published TFRs in Section 6, and we conclude in Section 7.

When needed, we assume a flat Λ CDM cosmology with $\Omega_M = 0.3151$ and $H_0 = 100h$ km/s/Mpc.

2. DARK ENERGY SPECTROSCOPIC INSTRUMENT

A multi-object fiber spectrograph installed on the Mayall 4-meter telescope at Kitt Peak National Observatory, the Dark Energy Spectroscopic Instrument (DESI; DESI Collaboration et al. 2022) is designed to efficiently conduct a large-scale redshift survey, collecting ~ 63 million redshifts over at least 17,000 sq. deg. of the sky in 8 years (DESI Collaboration et al. 2016a). DESI contains 5000 robotic fibers covering ~ 8 deg², enabling it to measure up to 5,000 spectra with a wavelength range of 3600–9800 Å in a single exposure (DESI Collaboration et al. 2016b; J. H. Silber et al. 2023; T. N. Miller et al. 2024; C. Poppett et al. 2024). The instrument was designed to allow each fiber to move anywhere within a patrol radius with minimal overlap of its neighboring fibers. DESI’s measured spectra are processed with Redrock⁴⁸, an offline spectroscopic pipeline using template-matching to extract redshifts (J. Guy et al. 2023).

We use the DESI Data Release 1 (DR1; DESI Collaboration et al. 2025) in this analysis, which contains the spectroscopic observations of 18.7 million objects made during the first year of DESI (Y1). DESI observes objects within one of three programs according to the current sky conditions and brightness of the sky (e.g., twilight, moon phase, dark sky); the programs are named “bright,” “dark,” and “backup” and are essentially treated independently. Because DESI is following a depth-first strategy, DR1 contains 41.3% of the bright survey (9739 sq. deg.) and 29.0% of the dark survey

⁴⁸ <https://github.com/desihub/redrock>

(9528 sq. deg.). For more details, see [DESI Collaboration et al. \(2025\)](#).

DESI was designed to make the most precise measurement of the expansion history of the Universe to determine the nature of dark energy using Baryonic Acoustic Oscillations (BAO; [M. Levi et al. 2013](#); [A. G. Adame et al. 2025a,b](#)). To do so, it makes use of several target classes/tracers in the main survey, selected from the DESI Legacy Imaging Surveys ([A. Dey et al. 2019](#)) with the DESI target selection pipeline ([A. D. Myers et al. 2023](#)): Bright Galaxies (BGS; [C. Hahn et al. 2023](#)), Luminous Red Galaxies (LRG; [R. Zhou et al. 2023](#)), Emission Line Galaxies (ELG; [A. Raichoor et al. 2023](#)), and Quasi-Stellar Objects (QSO; [E. Chaussidon et al. 2023](#)), as well as Milky Way stars (MWS; [A. P. Cooper et al. 2023](#)). These primary targets often do not make use of all 5000 fibers in a single tile (constructed using the optimized survey operations pipeline of [E. F. Schlafly et al. 2023](#)), so DESI fills the spare fibers with a number of secondary targeting programs designed by members of the DESI collaboration ([A. D. Myers et al. 2023](#)), increasing the scientific output. One of these programs is the DESI Peculiar Velocity Survey ([C. Saulder et al. 2023](#)).

2.1. The DESI Peculiar Velocity Survey

The DESI Peculiar Velocity (PV) Survey ([C. Saulder et al. 2023](#)) is a secondary targeting program of DESI that was designed to measure the peculiar velocities of galaxies in the local universe ($z \lesssim 0.15$). The addition of these peculiar motions will increase the precision of DESI’s measurement of $f\sigma_8$, the product of the redshift-dependent growth rate of structure (f) and the amplitude of the linear power spectrum on the scale of 8 Mpc/ h (σ_8). As described in Sec. 1, peculiar velocities can be measured when we know the galaxy’s observed redshift and its distance through some other, redshift-independent, method. The DESI PV Survey targets galaxies whose distances can be measured either via the Tully-Fisher Relation (late-type galaxies) or the Fundamental Plane (early-type galaxies). We focus on the DESI DR1 Tully-Fisher sample here; see [C. Ross et al. \(in prep.\)](#) for a complementary discussion of the DESI DR1 Fundamental Plane sample and its calibration, and see [C. Saulder et al. \(2023\)](#) for the DESI PV Survey’s target design.

Similar to [K. Douglass et al. \(2025\)](#), the late-type galaxies that comprise the TF sample are selected from the Siena Galaxy Atlas 2020 (SGA 2020; [J. Moustakas et al. 2023](#)). Constructed with the DESI Legacy Imaging Surveys DR9 ([A. Dey et al. 2019](#)) north of -30° declination, the SGA 2020 is a size-limited catalog con-

taining galaxies with diameters of the 25th magnitude arcsec^{-2} isophote, $D(25)$, greater than $20''$. Galaxies in the SGA 2020 are included in the TF sample if they have a Sersic index $n < 2$ (indicative of a spiral galaxy; [M. R. Blanton & J. Moustakas 2009](#)) and an inclination angle $> 20^\circ$ (an axis ratio, $b/a < 0.940$) as measured in the r -band. For each galaxy, the DESI PV Survey positions a fiber on the galaxy center and at a distance of $0.4R_{26}$ along the semimajor axis of the galaxy on either side of the center; R_{26} is the radius of the 26 mag arcsec^{-2} r -band isophote reported in the SGA 2020.

2.2. Photometric corrections

Similar to [K. Douglass et al. \(2025\)](#), we adjust the apparent magnitude of the galaxies to account for various systematics. If m_r is the magnitude within the 26-mag arcsec^{-2} isophote in the r -band as reported by the SGA-2020, then the corrected magnitude, $m_{r,\text{corr}}$ is

$$m_{r,\text{corr}} = m_r - A_{\text{MW dust}} - A_{\text{internal dust}} + A_k + A_{\text{sys}}. \quad (4)$$

Here, $A_{\text{MW dust}}$ is the Milky Way dust attenuation, $A_{\text{internal dust}}$ corrects for internal dust extinction, A_k is the k -correction, and A_{sys} adjusts for the offset between the two photometric surveys that comprise the DESI Legacy Surveys.

The extinction correction due to dust in the Milky Way is defined as

$$A_{\text{MW dust}} = R_r E(B - V), \quad (5)$$

where $R_r = 2.165$ and $E(B - V)$ is taken from the updated dust maps by [R. Zhou et al. \(2024\)](#). This correction is identical to that used in the DESI EDR TF calibration by [K. Douglass et al. \(2025\)](#).

We correct for the extinction due to internal dust within the target galaxy by removing the observed correlation between the apparent magnitude and axis ratio (shown in Fig. 1). The correction is defined as

$$A_{\text{internal dust}} = d \left(\frac{b}{a} - 1 \right) \quad (6)$$

where $d = -0.90^{+0.15}_{-0.18}$ is the slope of the line fit to the median magnitudes binned by the axis ratio. This is an updated correction to that used in the DESI EDR TF calibration [K. Douglass et al. \(2025\)](#), using the full DR1 TF sample.

Identical to [K. Douglass et al. \(2025\)](#), we adjust for the zero-point offset reported in [K. Said et al. \(2024\)](#) between the Beijing-Arizona Sky Survey (BASS; [H. Zou et al. 2017](#)) and the Mayall z -band Legacy Survey (MzLS; [A. Dey et al. 2019](#), at $\text{Dec} \geq +32.375^\circ$) and the Dark Energy Camera Legacy Survey (DECaLS;

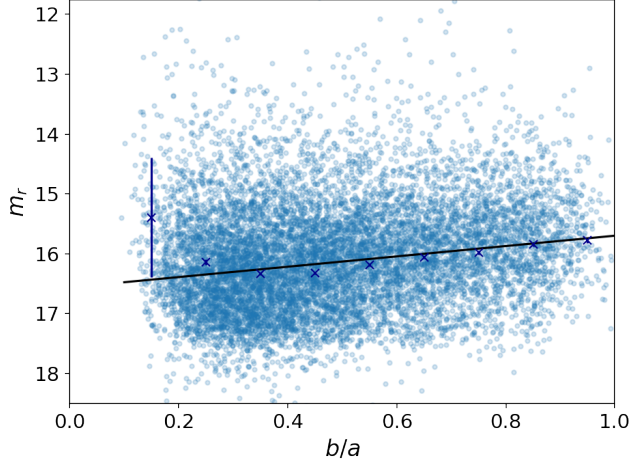


Figure 1. Observed correlation between r -band apparent magnitude and axis ratio. A linear fit to the median magnitudes in each bin (dark blue crosses) is shown in the black line.

B. Flaugher et al. 2015, for $\text{Dec} \geq +32.375^\circ$), the two photometric surveys that are used in the SGA 2020:

$$m_{r,\text{BASS}} - m_{r,\text{DECaLS}} = 0.0234 \quad (7)$$

with a root mean square (RMS) deviation of 0.02 mag and an error on the mean of 0.00049. As in K. Douglass et al. (2025), we adjust the BASS magnitudes to shift them into the DECaLS frame.

Finally, we K -correct the SGA 2020 magnitudes to a redshift of 0.1 using the `kcorrect` Python package (M. R. Blanton & S. Roweis 2007). Note that this is a different redshift than was used in the DESI EDR TF calibration (K. Douglass et al. 2025), but matches that used by C. Ross et al. (in prep.) in the DR1 FP calibration.

3. MEASURING THE ROTATIONAL VELOCITY

We compare the redshifts observed at the galaxy’s center and at $0.4R_{26}$ to estimate the rotational velocity of the galaxy, one of the two quantities in the TFR. For each galaxy, we measure the component of the rotational velocity along our line of sight, $V'(0.4R_{26})$, by removing the galaxy’s systemic motion (the redshift measured at the center of the galaxy) from the measured redshift at $0.4R_{26}$:

$$\frac{V'(0.4R_{26})}{c} = \frac{1 + z(0.4R_{26})}{1 + z_{\text{center}}} - 1 \quad (8)$$

The redshifts are measured from the spectra using Redrock, DESI’s redshift pipeline. Similar to the DESI EDR TF analysis (K. Douglass et al. 2025), we add a 7 km/s uncertainty in quadrature to each redshift uncertainty reported by Redrock to account for its precision

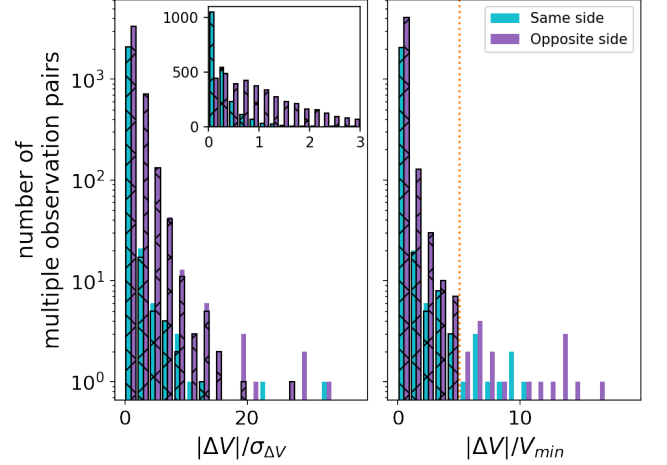


Figure 2. *Left:* Pull distribution of the difference in $V(0.4R_{26})$ for pairs of observations on the same galaxy (on the same or opposite side of the galaxy center). *Right:* Distribution in $\Delta V/V_{\min}$ for galaxies with multiple measures of $V(0.4R_{26})$. For a given galaxy, all its pairs must fall to the left of the dotted orange line for the galaxy to be in the final sample; those that do are shown in the black hashed histograms.

uncertainty. To recover the tangential rotational velocity at $0.4R_{26}$ from the component that we observe along the line of sight, we correct each measure of $V'(0.4R_{26})$ with the galaxy’s inclination angle:

$$V(0.4R_{26}) = \frac{V'(0.4R_{26})}{\sin i}. \quad (9)$$

We convert the galaxy’s photometric axis ratio from the SGA 2020, b/a , to the inclination angle as

$$\cos^2 i = \frac{(b/a)^2 - q_0^2}{1 - q_0^2}, \quad (10)$$

with $q_0 = 0.2$ (R. B. Tully & M. J. Pierce 2000).

We use the same quality criteria as with the DESI EDR TF calibration (K. Douglass et al. 2025):

- Center redshifts must have $\text{DELTA}12 > 25$ and $\text{ZWARN} = 0$;
- Measured rotational velocities $V(0.4R_{26})$ must be between 10–1000 km/s;
- When there are multiple measures of $V(0.4R_{26})$ for a given galaxy, only rotational velocities with $\text{DELTA}12 > 25$ that also satisfy $\Delta V/V_{\min} < 5$ are used, where ΔV is the difference between any two of the $V(0.4R_{26})$ and V_{\min} is the minimum $V(0.4R_{26})$ in that galaxy.

Uncertainties in $V(0.4R_{26})$ are estimated by propagating the redshifts uncertainties through Eqns. 8–9. Fig. 2

shows the pull distribution for ΔV (on the left) and $\Delta V/V_{\min}$ (on the right). As the inset on the left shows, our estimates on the velocity uncertainties are appropriate.

If a galaxy has multiple measures of $V(0.4R_{26})$ that pass all quality cuts, we use the weighted average of all the $V(0.4R_{26})$ as that galaxy’s rotational velocity.

3.1. Rotational velocity systematics

To confirm the accuracy with which we are recovering the rotational velocity with a single measurement along a galaxy’s major axis, we compare the velocities at $0.4R_{26}$ as measured in the DESI PV Survey to the rotational velocities at $0.4R_{26}$ based on models of H α velocity fields from the SDSS Mapping Nearby Galaxies at APO Survey (K. Bundy et al. 2015, MaNGA). We investigate the differences in velocities for 207 galaxies that are in the DR1 TF sample and are observed in SDSS MaNGA DR17 and modeled by N. Ravi et al. (2023), in order to evaluate the systematics associated with measuring velocities at $0.4R_{26}$.

3.1.1. SDSS MaNGA

SDSS MaNGA DR17 (Abdurro’uf et al. 2022) was the final data release of MaNGA, an integral field spectroscopy survey of $\sim 10,000$ galaxies. The MaNGA integral field units (IFUs) contain between 19 and 127 fibers covering $12.5''$ to $32.5''$ in diameter. The light received by the IFU was fed to two spectrographs with wavelength ranges of 3600–10,300 Å with a resolution of $\lambda/\Delta\lambda \sim 2000$ (S. A. Smeed et al. 2013). The SDSS MaNGA sample contains galaxies observed out to $1.5R_e$ or $2.5R_e$, where R_e is the half-light radius of a galaxy. Using two-dimensional H α velocity fields from SDSS MaNGA, N. Ravi et al. (2023) model the rotational velocity of ~ 5500 disk galaxies.

N. Ravi et al. (2023) fit the H α velocity maps from SDSS MaNGA to the following rotation curve parameterization (J. K. Barrera-Ballesteros et al. 2018):

$$V(r) = \frac{V_{\max} r}{(R_{\text{turn}}^\alpha + r^\alpha)^{1/\alpha}}. \quad (11)$$

$V(r)$ is the rotational velocity at distance r from the center of each galaxy. The parameterization describes a rotation curve where the velocity increases until distance R_{turn} from the center of the galaxy, turns with sharpness α , and plateaus at velocity V_{\max} . V_{\max} , R_{turn} , α , as well as the inclination angle i , the kinematic position angle ϕ , and the kinematic center of the galaxy are free parameters in the fit. See N. Ravi et al. (2023) for details of the modeling procedure.

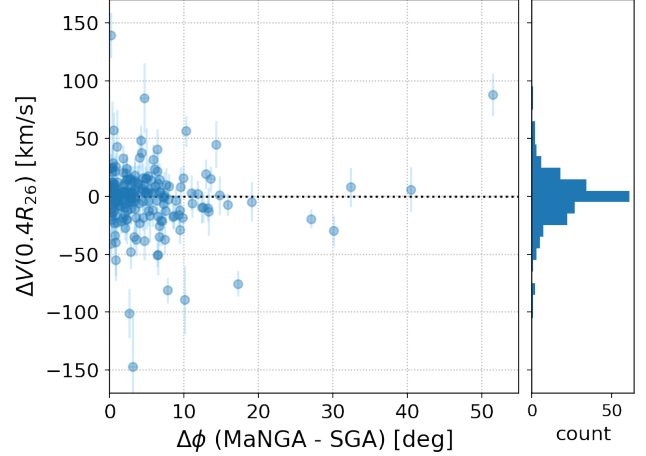


Figure 3. Difference in the velocity at $0.4R_{26}$ as measured in the DESI PV Survey and calculated from the SDSS MaNGA velocity field fits from N. Ravi et al. (2023) as a function of the difference in the photometric position angle from the SGA and the kinematic position angle from the velocity field fits from N. Ravi et al. (2023).

3.1.2. Kinematic v. photometric position angle

We investigate if the velocity measurements at $0.4R_{26}$ are affected by incorrect position angles by examining the difference between the velocity at $0.4R_{26}$ measured in the DESI PV survey and modeled by N. Ravi et al. (2023) as a function of the difference in the photometric position angle used for targeting in the DESI PV survey and the kinematic position angle from N. Ravi et al. (2023).

The DESI PV Survey uses the SGA’s photometric position angles ϕ , defined as the position of a galaxy’s major axis east of north, to place a DESI fiber at galactocentric radius $0.4R_{26}$ along a galaxy’s major axis. The rotational velocity calculated with Eqn. 9 needs to be corrected for the difference between the kinematic and photometric position angles.

In Fig. 3, we show the difference between the rotational velocity measurements at $0.4R_{26}$ from the DESI PV Survey and the rotational velocities at $0.4R_{26}$ obtained from the SDSS MaNGA velocity field modeling, $\Delta V(0.4R_{26})$, as a function of the difference between the photometric position angle from the SGA and the kinematic position angle from the fit by N. Ravi et al. (2023), $\Delta\phi$. We see no correlation between the difference in position angles and the difference in velocities. There are three galaxies with $\Delta V(0.4R_{26}) > 100$ km/s. Of these three, one galaxy has a velocity map that appears to be affected by the presence of an AGN. The other two galaxies are small in angular size compared with the

size of the DESI fiber, which may affect the velocity measurement.

3.1.3. Velocity dispersion introduced with DESI

We can compare the observed velocity at $0.4R_{26}$ in the DESI PV Survey to the predicted velocity at $0.4R_{26}$ from the rotation curve fits of [N. Ravi et al. \(2023\)](#) for galaxies observed in both the DESI PV Survey and SDSS MaNGA in order to understand the dispersion due to measuring the velocity at a single radius rather than over the face of each galaxy.

To remove the differences in velocities due to differences in the position angle and inclination angle between the SGA photometric fits and the best-fit values of [N. Ravi et al. \(2023\)](#), we first correct the predicted velocities at $0.4R_{26}$, V_{MaNGA} , from the SDSS MaNGA rotation curve fits. The corrected velocity $V_{\text{MaNGA, expected}}$, the velocity at $0.4R_{26}$ from the rotation curve fits using the orientation of the galaxy provided by the SGA, is calculated as follows.

$$V_{\text{MaNGA, expected}} = A(Q \sin i)B(\Delta\phi)V_{\text{MaNGA}}, \quad (12)$$

where

$$A(Q \sin i) = \frac{\sin i_{\text{MaNGA}}}{\sin i_{\text{SGA}}}, \quad (13)$$

and

$$B(\Delta\phi) = \cos(|\phi_{\text{MaNGA}} - \phi_{\text{SGA}}|). \quad (14)$$

Here, i_{MaNGA} and ϕ_{MaNGA} are the best-fit inclination position angle from [N. Ravi et al. \(2023\)](#) respectively. The photometric inclination angle and position angle from the SGA are denoted as i_{SGA} and ϕ_{SGA} .

In Fig. 4, we compare the velocity measured at $0.4R_{26}$ in the DESI PV Survey and the expected velocity from the SDSS MaNGA rotation curve fits. The velocities lie along the $y = x$ line with some scatter in the relation. We measure this scatter by calculating the perpendicular distance of each point to the $y = x$ line. The center figure of Fig. 4 shows the distribution of these distances normalized by the expected position on the $y = x$ line. The standard deviation of this distribution is 0.15.

4. CALIBRATING THE TULLY-FISHER RELATION

We calibrate the TFR (Eqn. 3) in the form

$$M_r = a \log \left(\frac{V}{V_0} \right) + b \quad (15)$$

where M_r is the absolute magnitude of the galaxy in the r -band within the 26-mag isophote, $\log V_0 = 2.18$ is the median value of $\log V(0.4R_{26})$ of the subset of galaxies used in the calibration, a is the slope of the TFR, and b is

the zero-point. As done in [K. Douglass et al. \(2025\)](#) with the DESI EDR TF relation, we use a non-zero value for $\log V_0$ to minimize the correlation between the calibrated slope and y -intercepts of the TFR.

Similar to [K. Douglass et al. \(2025\)](#), we calibrate the TFR using a subset of the full DR1 TF sample. To ensure that we have a reasonable estimate of $V(0.4R_{26})$, we require all calibration galaxies to:

- Have an inclination angle $i > 45^\circ$,
- Have a rotational velocity $70 \text{ km/s} < V(0.4R_{26}) < 300 \text{ km/s}$ and $\log V(0.4R_{26}) < 0.3(\mu(z_{\text{CMB}}) - 34 - 5 \log h) + 2$,
- Have an apparent magnitude m_r larger than the minimum of $(17.75, \mu(z_{\text{CMB}}) - 17 + 5 \log h)$,
- Have a spiral morphology (described in detail in Sec. 4.1 below), and
- Pass visual inspection,

where $\mu(z_{\text{CMB}})$ is the distance modulus based off the observed DESI redshift in the CMB frame. Introducing quality cuts that depend on an assumed cosmology does not affect our calibration because, as described in Sec. 4.2, we calibrate in redshift bins, so these criteria translate to a uniform cut in each bin that is consistent across all bins. The visual inspection is used to, for example, remove galaxies with either obvious tidal features or are overlapping another galaxy, or observations which are close to a bright star.

4.1. Identifying galaxy morphology

As the TFR is applicable only to galaxies supported against gravitational collapse by rotation (usually late-type spiral galaxies), we apply machine learning to develop an automated morphological classification system for the DESI DR1 TF galaxy sample to identify spiral galaxies. Using imaging from the DESI Legacy Surveys Data Release 9 (DR9; [A. Dey et al. 2019](#)), we adapt the pre-trained self-supervised model `ssl_legacysurvey` ([G. Stein et al. 2021](#)), which embeds galaxies in a high-dimensional latent space based on their color and morphology. The similarity search algorithm sorts images based on representations created from multiple augmentations of the original image, allowing the model to learn different morphological features. These learned representations are then projected to two dimensions using a Uniform Manifold Approximation and Projection (UMAP; [L. McInnes et al. 2018](#)), as shown in Fig. 5, to visualize morphological similarity.

To assign morphological classes to each galaxy, we construct a labeled anchor sample of 4,000 galaxies from

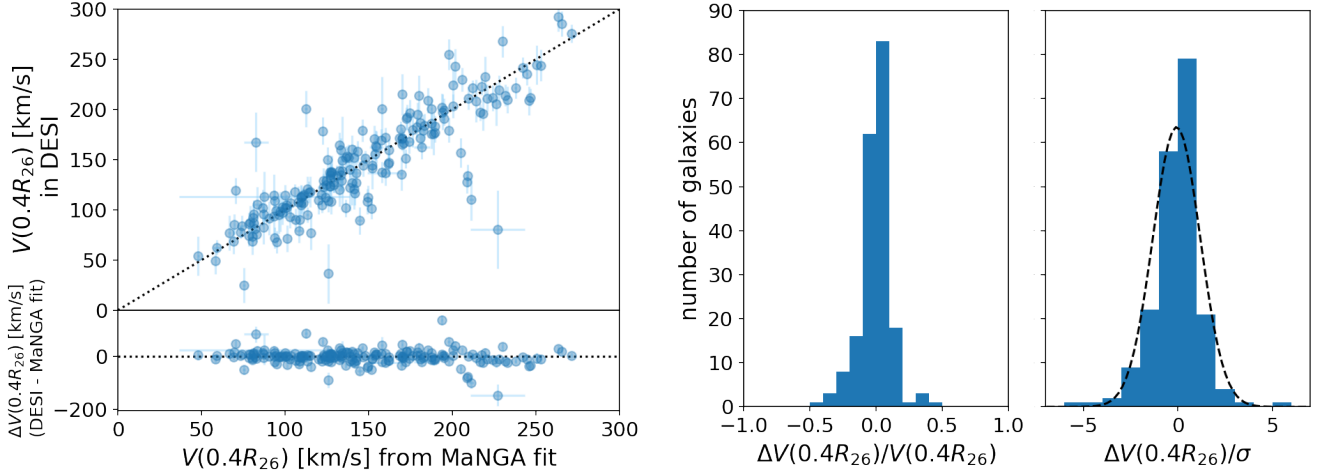


Figure 4. Rotational velocities at $0.4R_{26}$ as measured in the DESI PV Survey and calculated from the the SDSS MaNGA velocity field fits from [N. Ravi et al. \(2023\)](#) corrected for the differences in inclination and position angle between the two measurements. The left figure compares the two velocities with the black dotted line indicating where the velocities are equal. The center histogram shows the perpendicular distance of each galaxy to $y = x$, $\Delta V(0.4R_{26})$, normalized by the average of the two velocity measurements, the expected value on $y = x$. The right histogram shows the pull distribution of $\Delta V(0.4R_{26})$. The black dashed line shown a Gaussian fit to the pull distribution with a mean of -0.07 and standard deviation of 1.25 .

the SGA 2020, consisting of 1,000 visually-inspected galaxies for each of the following morphological types: Spiral, Elliptical, Lenticular, and Irregular. Galaxies were randomly selected from the SGA sample that had existing classifications in the HyperLeda catalog ([D. Makarov et al. 2014](#)). We visually inspected each selected galaxy to confirm its classification, building up an anchor sample of 1,000 galaxies of each type. During visual inspection, we use qualitative morphological criteria:

Spiral: The presence of a disk with visible spiral arms, and often a central bulge;

Elliptical: Smooth centrally concentrated light profiles with round or ellipsoidal shapes, and no visible spiral arms;

Lenticular: Smooth disk that lacks spiral arms and has a prominent central bulge;

Irregular: Disturbed asymmetric structure without a clear disk or bulge.

We then project the 10,262 unclassified galaxies from the DESI DR1 TF sample into the same UMAP space, shown in Fig. 5. Since morphological labels are assigned prior to the VI-based quality cuts, some of the UMAP cutouts may include bright stars or tidal features. We note that dwarf galaxies may also be present, but are removed from the final sample, as described in Sec. 5.1; the anchor galaxies were manually screened to avoid these cases. Next, we apply four separate binary k -nearest

neighbor classifiers (k-NN; [T. Cover & P. Hart 1967](#)), each trained to recognize one of the four morphological types. Each k-NN classifier evaluates whether a galaxy belonged to its target class by identifying the most similar labeled galaxies in the embedding and assigning a label based on the majority class among those neighbors.

We combine the four predictions to identify cases of agreement. Galaxies that receive a positive prediction from exactly one classifier were confidently assigned that morphological type, while ambiguous cases (those receiving multiple or no positive predictions) are left unlabeled. To improve coverage, we implement an iterative process. After each classification round, the remaining unclassified galaxies are re-projected using a new UMAP embedding alongside the fixed anchor set, and the k-NN classification is repeated. We performed three iterations in this analysis, with 5% remaining unclassified, typically due to their location near morphological boundaries in the embedding space.

Using this method, we achieve a mean classification accuracy of 82%, estimated via 5-fold cross-validation against the anchor point labels, and a completeness of 95% for the DESI DR1 TF sample. As described in the next section, galaxies must be positively identified as spirals with this classification technique to be used to calibrate the TFR. As described in [C. Saulder et al. \(2023\)](#), our sample selection for galaxies in the TF sample of the DESI PV Survey was designed to preferentially select spiral galaxies, so most of our sample is late-type spirals. However, there are some interloping lenticular galaxies, as well as some ellipticals and irregular galax-

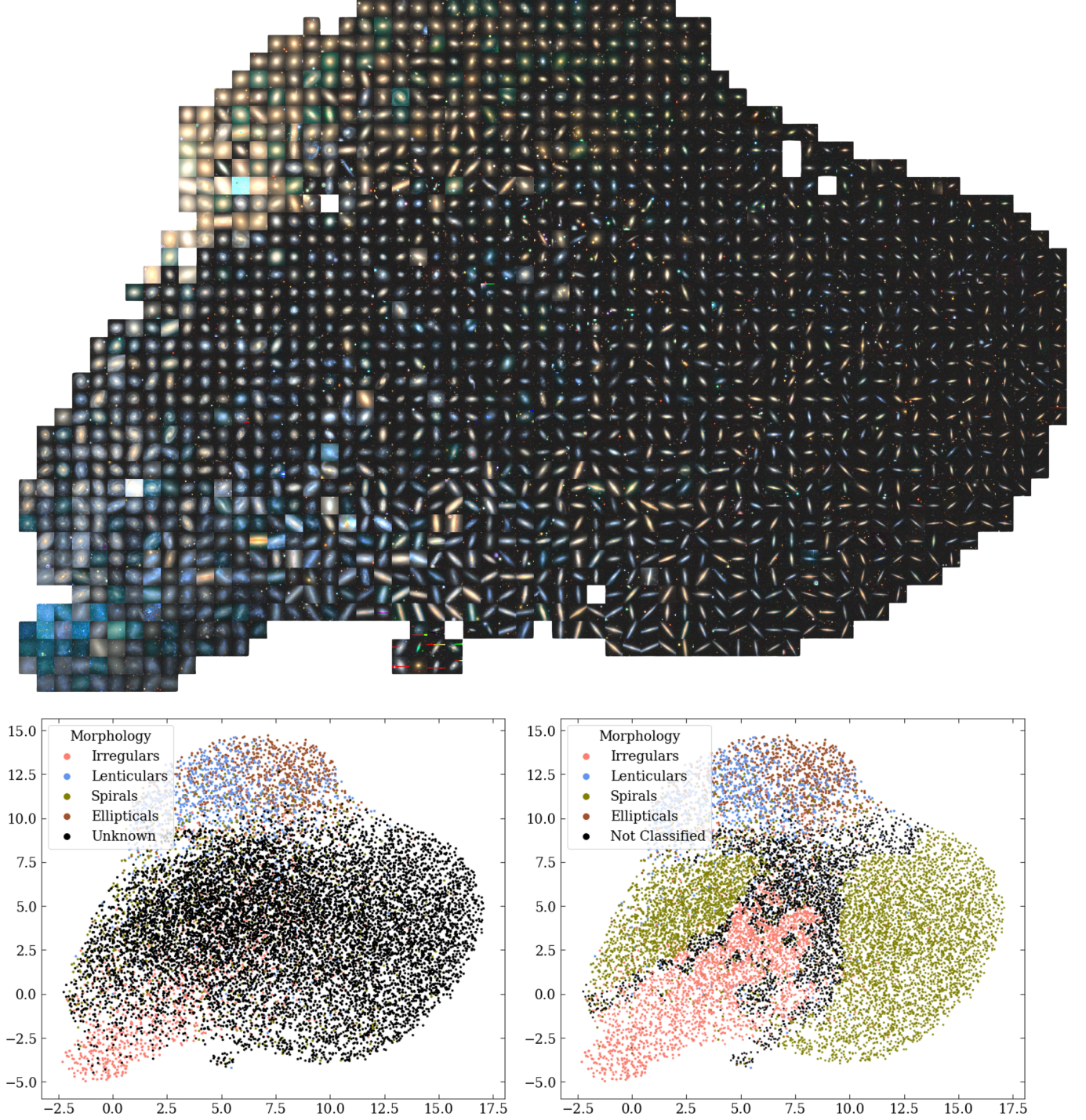


Figure 5. Uniform Manifold Approximation and Projection (UMAP) of the DESI DR1 TF sample. *Top:* We show the cutouts of a random subset of 1,718 galaxies from the full sample of 10,262 DESI DR1 TF galaxies + 4000 anchor galaxies, to demonstrate how the classifier sorts the galaxies by similar appearance. This subset of galaxies are a mix of galaxies with unknown classifications and anchor galaxies of Elliptical, Spiral, Lenticular, or Irregular classifications, as shown in the bottom left plot. *Bottom left:* Complete UMAP of the full 10,262 DESI DR1 TF sample (shown as black points) along with the 4000 anchor galaxies with known morphological classifications (Irregulars in pink, Lenticulars in blue, spirals in olive, and ellipticals in brown). A random subset of this projection is shown on top with cutouts of the galaxy images to show how the classifier sorts the images based on their appearance. We see that the anchor ellipticals are found grouped together towards the top right, anchor lenticulars in the top left, anchor irregulars in the bottom left, and anchor spirals are spread across the middle and right. The galaxies being classified (black points) sit primarily across the central and right regions of this projection, where the anchor spirals also sit, so the vast majority of the DESI DR1 TF sample are spiral galaxies. *Bottom right:* Result after the first classification iteration, showing the anchor galaxies and the newly classified galaxies in their corresponding colors. Those galaxies which have multiple potential classifications (because they sit in the overlap regions between the anchor points) are shown in black and will be evaluated in the second iteration.

ies. These comprise a relatively small fraction of the full DESI Y1 TF sample of 10,262 galaxies; we provide the SSL morphology classifications if a science application requires a pure spiral galaxy sample.

4.2. Defining galaxy samples for calibration

The TFR can be calibrated using either apparent or absolute magnitudes. To calibrate using apparent magnitudes requires knowing or assuming a distance to the galaxies *a priori*, severely limiting the sample size. Using the apparent magnitudes typically allows a larger sample of the galaxies to be used for calibration, but it requires grouping the galaxies so that all galaxies within a given subset are the same distance from us. This is typically done by assigning galaxies to clusters (e.g., E. Kourkchi et al. 2020a; K. Douglass et al. 2025), which requires a reliable cluster catalog and assumes that the TFR is the same in clusters as in the field (see, e.g., B. Milvang-Jensen et al. 2003; B. L. Ziegler et al. 2003; S. P. Bamford et al. 2005; O. Nakamura et al. 2006; P. Mocz et al. 2012, for studies assessing the accuracy of this assumption).

To avoid these requirements and use the largest possible set of galaxies for calibrating, we separate the galaxies into redshift bins of width $\Delta z = 0.005$ from $0.03 \leq z_{\text{CMB}} \leq 0.1$. The lower limit of our redshift range is chosen to avoid calibrating with galaxies whose peculiar velocities potentially comprise a significant fraction of their observed redshifts, and the upper limit is selected based on the maximum redshift used for the associated cosmological analysis. There are a total of 4050 galaxies among these 14 redshift bins, with between 116 and 356 galaxies in each bin. See Table 1 for the number of galaxies in each redshift bin.

4.3. Joint calibration of the Tully-Fisher Relation

We perform a joint fit of the galaxies in each of the redshift bins, requiring all bins to share the same slope, but each to have its own y -intercept. (The y -intercepts will vary from bin to bin as they are in apparent-magnitude space, which is a function of distance.) We use the subclassed HyperFit⁴⁹ package (A. S. G. Robotham & D. Obreschkow 2015) that was used in K. Douglass et al. (2025) to perform the fit so that we can account for the residual scatter in the TFR. We are fitting a hybrid of both the TFR and inverse TFR, as HyperFit minimizes the distance perpendicular to the best-fit line:

$$m_r = a \log \left(\frac{V}{V_0} \right) + b_i, \quad (16)$$

Table 1. Number of calibration galaxies in each redshift bin

Redshift range	Number of galaxies	rms scatter [AB mag]
0.030–0.035	338	0.55
0.035–0.040	309	0.60
0.040–0.045	323	0.56
0.045–0.050	350	0.60
0.050–0.055	356	0.60
0.055–0.060	312	0.57
0.060–0.065	328	0.61
0.065–0.070	317	0.60
0.070–0.075	294	0.56
0.075–0.080	297	0.61
0.080–0.085	303	0.59
0.085–0.090	242	0.50
0.090–0.095	165	0.66
0.095–0.100	116	0.46

where b_i is the y -intercept for the i^{th} redshift bin, by maximizing the log-likelihood

$$\ln \mathcal{L} = \frac{1}{2} \sum_{i=1}^{14} \sum_{j=1}^{N_i} \left[\ln \left(\frac{a^2 + 1}{s_j^2} \right) - \frac{\left(a \log \left(\frac{V_j}{V_0} \right) + b_i - m_{r,j} \right)^2}{s_j^2} \right], \quad (17)$$

where $s_j^2 = \sigma^2 + \sigma_{\log(V_j)}^2 a^2 + \sigma_{m_{r,j}}^2$ and N_i is the number of galaxies in the i^{th} redshift bin. We have 16 free parameters: the slope a , the y -intercepts $b_{1...14}$ for each of the 14 redshift bins, and the intrinsic scatter of the TFR, σ .

Fig. 6 shows the TFR for our 4050 calibration galaxies in the 14 redshift bins, with a best-fit slope value of -7.22 ± 0.01 AB mag. The intrinsic scatter along the magnitude axis for the sample of calibration galaxies is 0.466 ± 0.001 AB mag, comparable to that found in earlier TF calibrations (e.g., 0.41 mag and 0.49 mag in R. B. Tully & H. M. Courtois 2012; E. Kourkchi et al. 2020a, respectively). The corner plot for the TFR calibration is shown in Fig. 7.

5. MEASURING PECULIAR VELOCITIES

The peculiar velocity of a galaxy alters its observed redshift, so the difference between the inferred and predicted galaxy distance moduli can be attributed to the

⁴⁹ Available at <https://github.com/CullanHowlett/HyperFit>

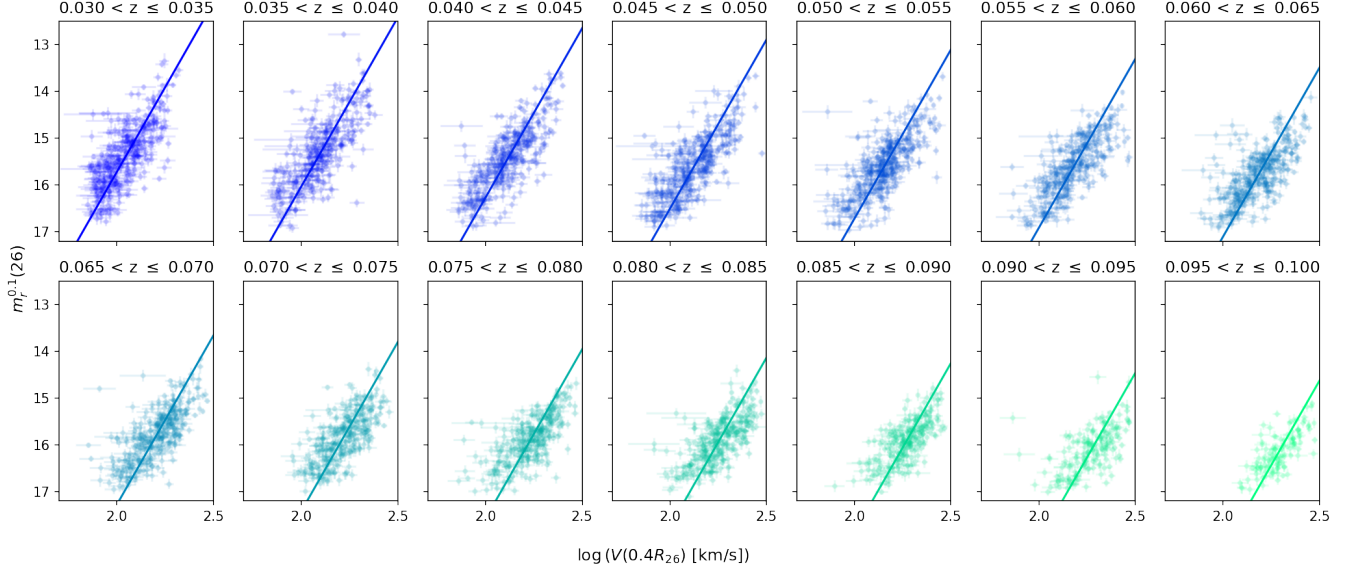


Figure 6. The 4050 DESI DR1 galaxies used for calibrating the TFR, shown in redshift bins $0.03 < z_{\text{CMB}} < 0.1$ of width $\Delta z = 0.005$. The calibrated TFR for each redshift bin is drawn with the colored solid lines. The slope of the TFR is the same across all bins, but each redshift bin has its own y -intercept. The apparent magnitudes used for calibration are from Eqn. 4, which have been K -corrected to $z = 0.1$.

peculiar velocity, along with some scatter that averages out over a large enough sample. We use the calibrated TFR to estimate the distance modulus, μ_{TF} , given a galaxy’s observed rotational velocity. We convert the calibrated y -intercepts of the TFR in each redshift bin to an absolute magnitude using the central redshift of the bin, $z_{c,i}$, so that

$$B_i = b_i - \mu(z_{c,i}) \quad (18)$$

A galaxy’s predicted absolute magnitude is then calculated from the calibrated TFR as

$$M_r = a \log \left(\frac{V(0.4R_{26})}{V_0} \right) + B_i \quad (19)$$

using the B_i of the redshift bin within which the galaxy falls. We use the B_i of the lowest redshift bin for those galaxies with $z < 0.03$, and we use the B_i of the highest redshift bin for those galaxies with $z > 0.1$. The TFR for the 10,262 galaxies in the DESI DR1 TF sample is shown in Fig. 8, where the absolute magnitudes for each object are calculated using the proper distance for a flat Λ CDM cosmology with $\Omega_M = 0.3151$, $H_0 = 100h$ km/s/Mpc using the DESI DR1 redshift of the center of the galaxy.

The effect of peculiar velocities directly on the observed magnitude of the galaxy is subdominant to the effect on redshift and intrinsic scatter of the TFR. We extract the PV information by comparing the inferred distance modulus, $\mu(z_{\text{CMB}})$, with that predicted by the TFR, μ_{TF} , where

$$\mu_{\text{TF}} = m_{r,\text{corr}} - M_{r,\text{TF}}, \quad (20)$$

to compute the log distance ratio,

$$\eta = 0.2 (\mu(z_{\text{CMB}}) - \mu_{\text{TF}}). \quad (21)$$

We choose to quantify the peculiar velocities with the log distance ratio because its errors are Gaussian-distributed. In Fig. 9, we show the weighted mean log distance ratio as a function of the redshift for the DESI DR1 TF sample. The distance moduli and log distance ratios for the DESI DR1 TF sample are shown in Table 2, and the distributions of the log distance ratios and their uncertainties are shown in Fig. 10.

5.1. Defining the main TF sample

As is apparent in Fig. 8, the DESI DR1 TF sample has significant scatter, particularly above and to the left of the TFR. These correspond to lower rotational velocities measured than what one would expect from the observed redshift and apparent magnitude. One possibility for their underestimated rotational velocities is if their rotation curves have not reached the maximum velocity by $0.4R_{26}$. As these objects will bias some studies using this sample, we extend a subset of our requirements for the calibration sample to the full TF sample, defining the main cosmology sample as those with

- A rotational velocity $70 \text{ km/s} < V(0.4R_{26}) < 300 \text{ km/s}$ and $\log V(0.4R_{26}) < 0.3(\mu(z_{\text{CMB}}) - 34 - 5 \log h) + 2$, and
- An apparent magnitude m_r larger than the minimum of $(17.75, \mu(z_{\text{CMB}}) - 17 + 5 \log h)$ (i.e., non-dwarf galaxies).

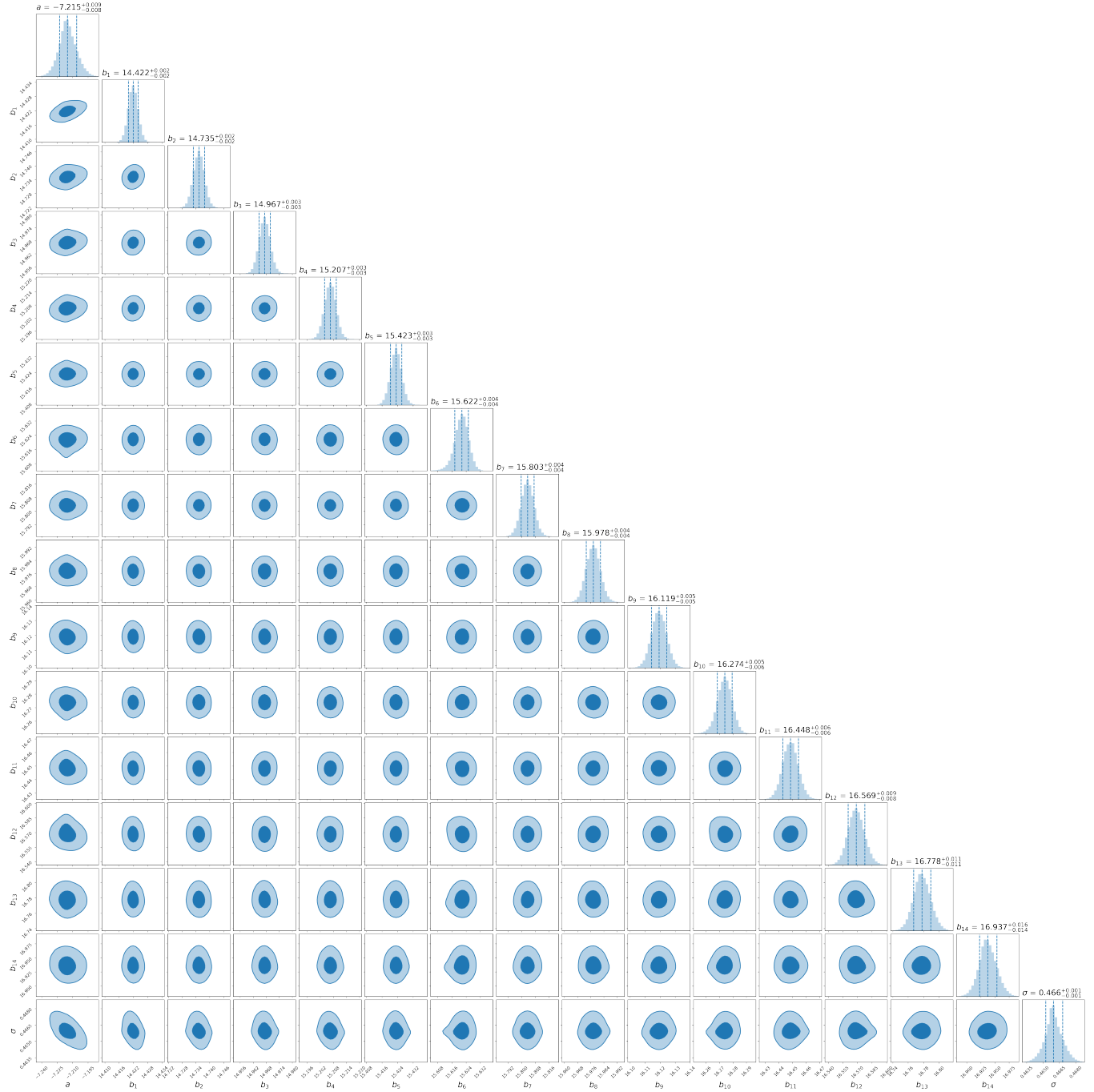


Figure 7. Corner plot of the linear fits to the galaxies in the redshift bins shown in Fig. 6, where a is the slope, b_i for $i = 1 \dots 14$ is the y -intercept of the each bin’s TFR, and σ is the intrinsic scatter along the magnitude axis.

Galaxies in the DESI DR1 TF sample which are part of this main population are shown in the colored density bins in Fig. 8, while those that are not are shown as grey points. The distribution of the TF galaxies in DESI DR1 on the sky is shown in Fig. 11, and the $N(z)$ distribution of the DESI DR1 TF sample is shown in Fig. 12.

5.2. Constructing the clustering catalogs

The positions and velocities of the DESI DR1 TF galaxy sample are used in subsequent analysis to constrain the growth rate of structure (R. Turner et al. in prep.; F. Qin et al. in prep.; Y. Lai et al. in prep.). For the purposes of these clustering measurements, we define a subsample of the DR1 TF catalog that is restricted to the most reliable peculiar velocity measurements, and

Table 2. DESI DR1 TF catalog

SGA-2020 ID	R.A. [deg]	Decl. [deg]	Redshift	$D(26)$ [arcmin]	$m_r(26)$ [AB mag]	$V(0.4R_{26})$ [km/s]	μ [AB mag]	η	Main sample
38	211.6620	39.5272	0.0809(3)	0.42	17.50 ± 0.03	122 ± 11	36.72 ± 0.54	0.07 ± 0.11	True
55	199.7306	1.7263	0.0440(3)	0.50	17.58 ± 0.02	81.5 ± 9.0	35.60 ± 0.57	0.03 ± 0.11	True
117	138.9354	2.6948	0.0900(4)	0.57	16.68 ± 0.03	181 ± 14	37.08 ± 0.52	0.05 ± 0.10	True
223	197.7870	34.1713	0.0340(3)	0.58	17.34 ± 0.02	70 ± 12	34.82 ± 0.72	0.07 ± 0.14	True
581	118.8598	18.9755	0.0433(3)	0.95	16.19 ± 0.02	134 ± 11	35.46 ± 0.53	0.04 ± 0.11	True
669	198.7851	3.2186	0.0835(3)	0.62	15.86 ± 0.01	293 ± 17	38.14 ± 0.48	-0.20 ± 0.10	True
731	334.3157	-0.0666	0.0771(3)	0.56	17.55 ± 0.02	82 ± 12	35.42 ± 0.65	0.30 ± 0.13	True
1135	125.6008	7.0371	0.0788(3)	0.50	16.20 ± 0.02	218.7 ± 7.0	37.40 ± 0.46	-0.08 ± 0.09	True
1158	162.9366	3.0996	0.0464(2)	0.78	15.61 ± 0.02	178 ± 11	35.95 ± 0.49	-0.02 ± 0.10	True
1287	209.9386	-3.0886	0.0263(3)	0.71	16.12 ± 0.01	109 ± 20	35.09 ± 0.74	-0.10 ± 0.15	True

NOTE—Ten of the 10,262 galaxies in the DESI DR1 TF catalog. Sky positions and diameters of the 26 mag arcsec⁻² r -band isophote are from the SGA-2020 (J. Moustakas et al. 2023). Redshifts are measured from the DESI DR1 spectra, and rotational velocities at $0.4R_{26}$ are computed as described in Sec. 3. Distance moduli are calculated from the calibrated TFR, and the log distance ratios are based on the difference between the observed and predicted distance moduli. Table 2 is published in its entirety online in a machine-readable format. A portion is shown here for guidance regarding its form and content.

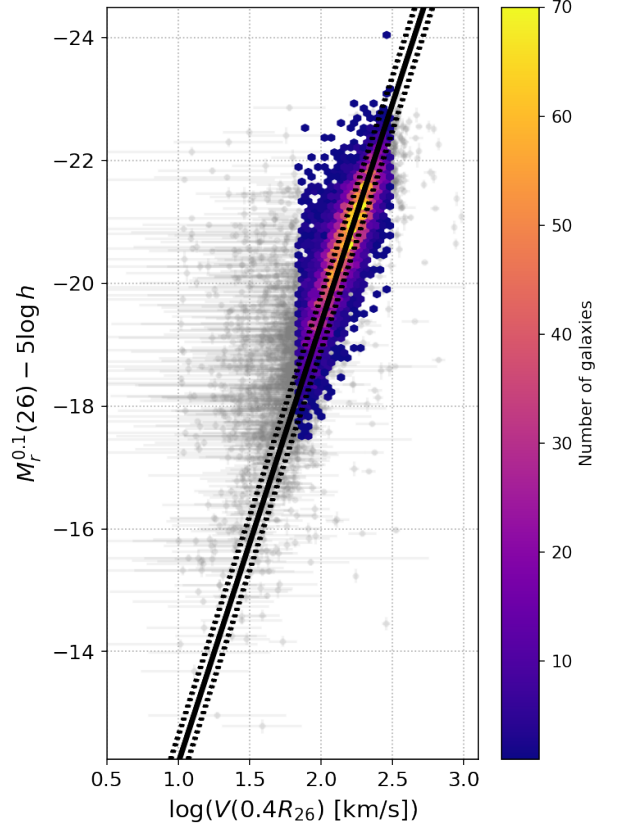


Figure 8. TFR of the DESI DR1 PV Survey galaxies, using the corrected absolute magnitudes described by Eqn. 4 that have been k -corrected to $z = 0.1$. Our calibrated TFRs are shown in the thick solid black line, and the intrinsic dispersion of the calibrated TFR is shown with the black dotted lines. Galaxies shown in gray are those which are not part of the main cosmological sample, due either to being considered dwarfs or not satisfying the velocity criteria described in Sec. 5.1. Galaxies are scattered vertically in this diagram due to their peculiar motion.

those where we have better knowledge of the systematic impact of the DESI fiber-assignment process, density variations in the imaging used for target selection, and redshift failures.

We do this by first restricting to galaxies in the main TF sample (i.e., those shown in the colored density bins in Figs. 8–9 and described in Sec. 5.1). We then cross-match these TF galaxies to a $z < 0.1$ sample of the BGS large-scale structure (LSS) catalogs presented in A. J. Ross et al. (2025) using each galaxy’s TARGETID. This restricts the TF data to only those objects within the well-defined angular mask of the LSS catalogs and allows us to borrow from those catalogs systematic weights accounting for completeness, imaging density fluctuations, and redshift success. In doing this cross-match, we identify 31 galaxies where the redshifts reported for

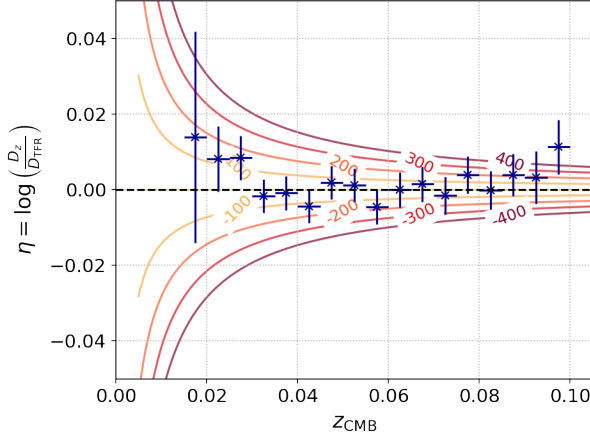


Figure 9. The weighted average log-distance ratio versus redshift for the DESI DR1 PV Survey TF sample. Lines of constant peculiar velocity are shown in shades of orange/red.

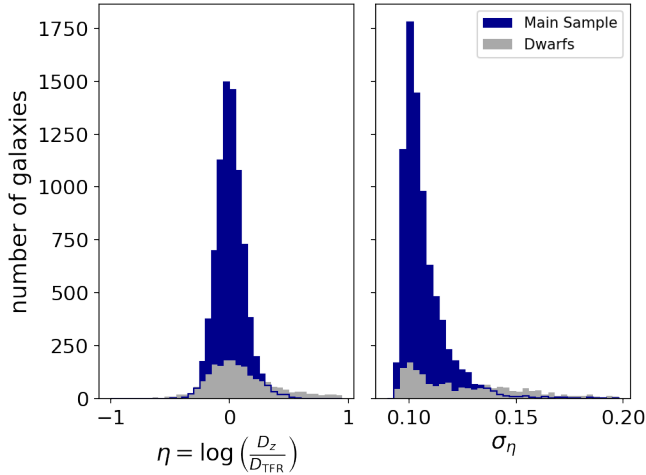


Figure 10. Distributions of the log-distance ratio (left) and uncertainty in the log-distance ratio (right) for the DESI DR1 PV Survey TF sample. Galaxies shown in gray are those which are not part of the main cosmological sample as defined in Sec. 5.1.

the galaxy in the BGS LSS catalogs differ by more than 10^{-4} from that given in the TF sample — these arise because the redshift reported in the TF catalog is an average over all measurements taken at the center of that galaxy in both bright and dark conditions, while those in the BGS LSS catalog use only bright time measurements. We elect to remove these galaxies from the clustering catalog rather than adopt either choice of redshift.

The end result is a subset of 6,807 galaxies (out of the full 10,262) that we use for subsequent clustering measurements. For this subset, we also produce random unclustered catalogs, with 20, 200, and 400 \times the

number of real galaxies with the same angular, redshift, and peculiar velocity error distributions. These are used to calculate and report the number density of BGS redshifts and TF-based peculiar velocity measurements at each TF galaxy’s position in the clustering catalog (used e.g., for measurements of the density and velocity power spectra in F. Qin et al. in prep.). The clustering catalog and associated random catalogs are released along with the full TF sample.

6. DISCUSSION

6.1. Comparison with CosmicFlows-4

We can compare our TFR calibration with the Cosmicflows-4 TFR (CF4; E. Kourkchi et al. 2020a) for those objects in our sample that have velocity widths measured in the ALFALFA H I survey (M. P. Haynes et al. 2018). While each of these catalogs contains $\sim 10,000$ galaxies, ours covers a much smaller portion of the sky and extends to much higher redshifts (3580 sq. deg., $z \lesssim 0.1$) than CF4 (almost full-sky, $z < 0.05$). We show how our distance moduli compare with those assigned distance moduli in E. Kourkchi et al. (2020b) in Fig. 13 for the 299 galaxies which are in both samples (96 of which are in our main cosmology sample), and we include the cross-matched sample in Table 3. The error bars shown in the figure, both the statistical (object-dependent) and systematic, reveal that our uncertainties are comparable to those of CF4. After accounting for the different H_0 values used in the two catalogs, we find relatively good agreement with the CF4 TFR. We note a slight bias of 0.21 ± 0.71 towards our TFR predicting larger distance moduli, which we attribute to an offset in the zero-pointing of the two TFRs. Of the three extreme outliers seen in Fig. 13, we find one to have a significantly different redshift ($\Delta z > 0.05$) between CF4 and DESI; the other two appear to have much larger H I velocities relative to $V(0.4R_{26})$, making them outliers in the H I TFR. Visual inspection of their Legacy Surveys images and DESI DR1 spectra reveal no anomalies.

6.2. Anchoring the zero-point of the TFR

The final step of calibrating the TFR is tying the zero-points in each redshift bin of the TFR to external calibrators with known independent distances. The zero-points B_i are unanchored and set such that the redshift-binned average distance modulus is 0 under the assumption that there is no average radial peculiar velocity over large sky areas. This global zero-pointing results in an offset

$$b_{0\text{pt}} = \Delta\mu_{0\text{pt}} = \langle\mu\rangle_{\text{TF}} - \langle\mu\rangle_{\text{ext}} \quad (22)$$

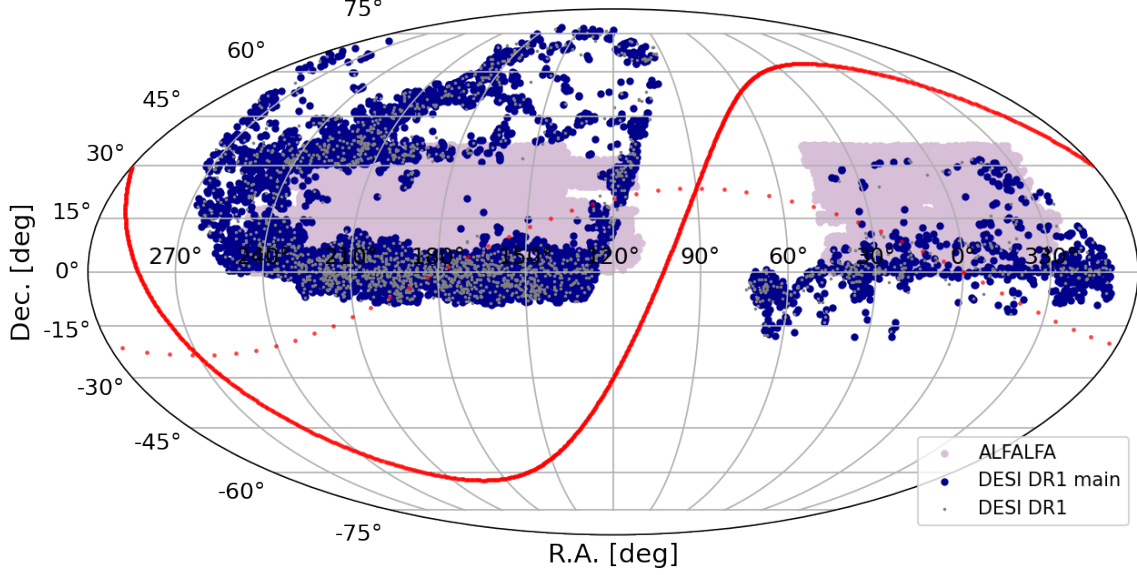


Figure 11. The distribution of Tully Fisher galaxies within the DESI DR1 dataset, presented here in a Mollweide projection. The purple shaded region corresponds to the ALFALFA (M. P. Haynes et al. 2018) footprint, and the red solid line represents the plane of the Milky Way. The main DESI DR1 TF sample is shown in dark blue, with those that do not satisfy the more stringent velocity and/or magnitude requirements shown in grey.

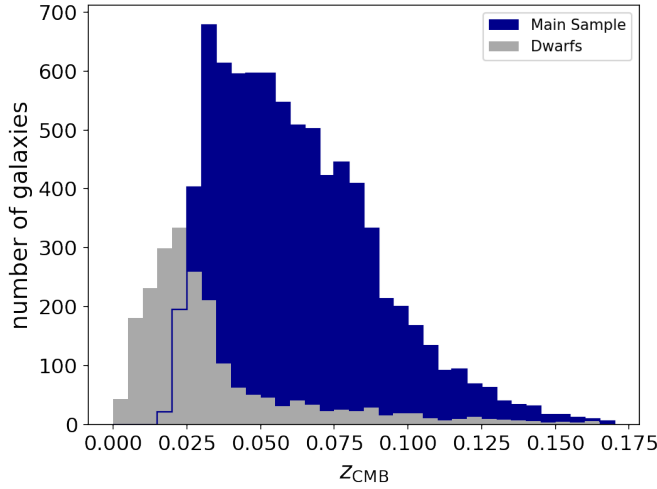


Figure 12. Redshift distribution of galaxies in the DESI DR1 PV Survey TF sample. The main DESI DR1 TF sample is shown in dark blue, with those that do not satisfy the more stringent velocity and/or magnitude requirements shown in grey.

to the TF Hubble diagram. A joint fit of the DESI DR1 TF, FP, and supernova Ia distances from the SH0ES/Pantheon+ sample (A. G. Riess et al. 2022; D. Brout et al. 2022) is performed to find the global zero-point. To improve the statistical uncertainty of the zero-point, we take advantage of galaxy groups to increase the overlap of supernova distance measurements with DESI

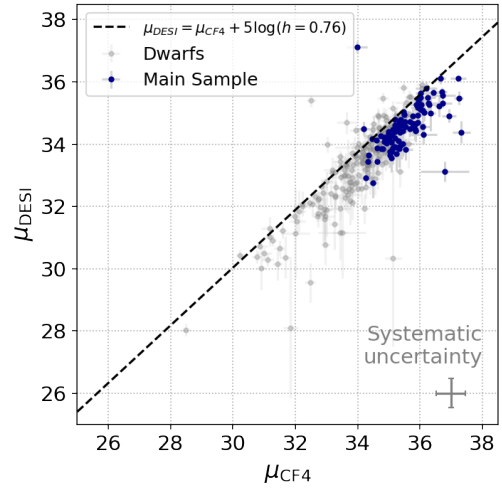


Figure 13. A comparison between the distance moduli from our calibrated TFR and that of Cosmicflows-4 (CF4; E. Kourkchi et al. 2020a). Galaxies that are not part of our main sample (defined in Sec. 5.1) are shown in grey. $y = x$ is shown in the black dashed line, adjusted for the value of H_0 used in both catalogs. We find relatively good agreement with CF4, with a slight bias towards larger distance moduli (0.21 ± 0.71).

DR1 PV Survey galaxies. The method of zero-pointing the TF and FP samples is described in detail in A. Carr et al. (in prep.), including a description of the galaxy group catalog and H_0 constraints that follow from the zero-pointed distance-redshift relation.

Table 3. DESI DR1 – CF4 cross-matched catalog

SGA-2020 ID	R.A. [deg]	Decl. [deg]	Redshift	$D(26)$ [arcmin]	m_r (DESI) [AB mag]	m_r (CF4) [AB mag]	$V(0.4R_{26})$ (DESI) [km/s]	W_{mx} (CF4) [km/s]	μ (DESI) [AB mag]	μ (CF4) [AB mag]	Main sample
2733	224.5346	3.4236	0.02150(2)	1.42	14.91 ± 0.02	14.7	119.9 ± 9.8	257 ± 5	33.84 ± 0.55	34.39 ± 0.48	False
15509	141.0202	2.1216	0.03687(2)	1.31	14.76 ± 0.01	14.7	191.3 ± 7.5	415 ± 29	35.32 ± 0.49	36.73 ± 0.54	True
18021	211.6584	3.7487	0.04059(3)	1.75	14.39 ± 0.01	14.5	212 ± 13	425 ± 12	35.31 ± 0.52	36.28 ± 0.49	True
23113	329.6040	-0.7397	0.01627(8)	1.40	15.00 ± 0.00	14.6	101 ± 25	179 ± 18	33.64 ± 0.97	34.26 ± 0.61	False
24070	347.3241	0.0643	0.01574(2)	1.28	15.19 ± 0.03	15.2	107 ± 13	270 ± 8	33.64 ± 0.62	34.29 ± 0.48	False

NOTE—Five of the 299 galaxies that contain data from both DESI DR1 and Cosmiflows4. Sky positions and diameters of the 26 mag arcsec⁻² r -band isophote are from the SGA-2020 (J. Moustakas et al. 2023). Redshifts are measured from the DESI DR1 spectra, rotational velocities at $0.4R_{26}$ are computed as described in Sec. 3, and distance moduli are calculated from the calibrated TFR. The CF4 values are from Tables 1 and 4 of E. Kourkchi et al. (2020b). Table 3 is published in its entirety online in a machine-readable format. A portion is shown here for guidance regarding its form and content.

7. CONCLUSION

We calibrate the Tully-Fisher relation (TFR) using galaxies observed in the first data release (DR1) of DESI’s eight year survey, targeted as part of DESI’s Peculiar Velocity Survey. This secondary targeting program measures the rotational velocities of 10,262 galaxies at $0.4R_{26}$ by placing fibers on the centers and major axes of spatially-resolved galaxies (primarily spirals) within the DESI footprint.

We fit for the TFR using 4050 galaxies across 14 redshift bins of width $\Delta z = 0.005$ from $0.03 < z < 0.10$ with 16 free parameters: the slope, y -intercepts of each of the 14 bins, and the intrinsic scatter in the TFR. We find a slope of -7.22 ± 0.01 AB mag in the r -band for velocities at $0.4R_{26}$, and an intrinsic scatter of the TFR of 0.466 ± 0.001 AB mag.

Our calibrated TFR allows us to measure the peculiar velocity of 10,262 galaxies observed as part of the DESI PV Survey DR1 TF sample. While the target selection used to define this sample of 10,262 galaxies was designed to identify late-type spiral galaxies, we find some interloping ellipticals, lenticulars, and irregular galaxies. We provide morphological classifications from a self-supervised learning algorithm for the 10,262 galaxies for further sample refinement. Along with the Fundamental Plane sample of the DESI PV Survey DR1 (C. Ross et al. in prep.), we use these peculiar velocities to study the growth rate of structure (R. Turner et al. in prep.; F. Qin et al. in prep.; Y. Lai et al. in prep.) and estimate the value of the Hubble constant, H_0 (A. Carr et al. in prep.). This TF catalog comprises $\sim 20\%$ of the full catalog expected by the completion of the full 8-year DESI PV Survey, which will comprise the largest catalog of TF distances to date. The substantial increase in sample size will greatly reduce the statistical uncertainties in the measured PVs of the sample, significantly contributing to the overall increase in precision of the growth rate of structure forecast for the DESI PV Survey (C. Saulder et al. 2023) in the local universe. We will also be able to study the systematics of the TFR in unprecedented detail with these future samples, increasing our understanding of the TFR and its use in measuring distances.

DATA AVAILABILITY

Data shown in figures, as well as example Python code to generate the figures, will be available on Zenodo upon acceptance.

ACKNOWLEDGEMENTS

The authors thank former undergraduate students Hayley Nofi (Villanova University), MJ Keller (University of Rochester), and Sunny Woo (University of Rochester) for their help in various stages of this analysis. This material is based on work supported in part by the National Science Foundation Grant No. PHY-2149332.

This material is based upon work supported by the U.S. Department of Energy (DOE), Office of Science, Office of High-Energy Physics, under Contract No. DE-AC02-05CH11231, and by the National Energy Research Scientific Computing Center, a DOE Office of Science User Facility under the same contract. Additional support for DESI was provided by the U.S. National Science Foundation (NSF), Division of Astronomical Sciences under Contract No. AST-0950945 to the NSF's National Optical-Infrared Astronomy Research Laboratory; the Science and Technology Facilities Council of the United Kingdom; the Gordon and Betty Moore Foundation; the Heising-Simons Foundation; the French Alternative Energies and Atomic En-

ergy Commission (CEA); the National Council of Humanities, Science and Technology of Mexico (CONAH-CYT); the Ministry of Science, Innovation and Universities of Spain (MICIU/AEI/10.13039/501100011033), and by the DESI Member Institutions: <https://www.desi.lbl.gov/collaborating-institutions>. Any opinions, findings, and conclusions or recommendations expressed in this material are those of the author(s) and do not necessarily reflect the views of the U. S. National Science Foundation, the U. S. Department of Energy, or any of the listed funding agencies.

The authors are honored to be permitted to conduct scientific research on I'oligam Du'ag (Kitt Peak), a mountain with particular significance to the Tohono O'odham Nation.

Software: Astropy (Astropy Collaboration et al. 2013, 2018, 2022), Corner (D. Foreman-Mackey 2016), HyperFit (A. S. G. Robotham & D. Obreschkow 2015), Kcorrect (M. R. Blanton & S. Roweis 2007), Matplotlib (J. D. Hunter 2007), NumPy (C. R. Harris et al. 2020), SciPy (P. Virtanen et al. 2020)

REFERENCES

- Abdurro'uf, Accetta, K., Aerts, C., et al. 2022, ApJS, 259, 35, doi: [10.3847/1538-4365/ac4414](https://doi.org/10.3847/1538-4365/ac4414)
- Adame, A. G., Aguilar, J., Ahlen, S., et al. 2025a, JCAP, 2025, 028, doi: [10.1088/1475-7516/2025/07/028](https://doi.org/10.1088/1475-7516/2025/07/028)
- Adame, A. G., Aguilar, J., Ahlen, S., et al. 2025b, JCAP, 2025, 028, doi: [10.1088/1475-7516/2025/07/028](https://doi.org/10.1088/1475-7516/2025/07/028)
- Astropy Collaboration, Robitaille, T. P., Tollerud, E. J., et al. 2013, A&A, 558, A33, doi: [10.1051/0004-6361/201322068](https://doi.org/10.1051/0004-6361/201322068)
- Astropy Collaboration, Price-Whelan, A. M., Sipőcz, B. M., et al. 2018, AJ, 156, 123, doi: [10.3847/1538-3881/aabc4f](https://doi.org/10.3847/1538-3881/aabc4f)
- Astropy Collaboration, Price-Whelan, A. M., Lim, P. L., et al. 2022, ApJ, 935, 167, doi: [10.3847/1538-4357/ac7c74](https://doi.org/10.3847/1538-4357/ac7c74)
- Bamford, S. P., Milvang-Jensen, B., Aragón-Salamanca, A., & Simard, L. 2005, MNRAS, 361, 109, doi: [10.1111/j.1365-2966.2005.09135.x](https://doi.org/10.1111/j.1365-2966.2005.09135.x)
- Barrera-Ballesteros, J. K., Heckman, T., Sánchez, S. F., et al. 2018, ApJ, 852, 74, doi: [10.3847/1538-4357/aa9b31](https://doi.org/10.3847/1538-4357/aa9b31)
- Bautista et al., J. in prep.
- Blanton, M. R., & Moustakas, J. 2009, ARA&A, 47, 159, doi: [10.1146/annurev-astro-082708-101734](https://doi.org/10.1146/annurev-astro-082708-101734)
- Blanton, M. R., & Roweis, S. 2007, AJ, 133, 734, doi: [10.1086/510127](https://doi.org/10.1086/510127)
- Bottinelli, L., Gouguenheim, L., Paturel, G., & de Vaucouleurs, G. 1983, A&A, 118, 4
- Brout, D., Scolnic, D., Popovic, B., et al. 2022, ApJ, 938, 110, doi: [10.3847/1538-4357/ac8e04](https://doi.org/10.3847/1538-4357/ac8e04)
- Bundy, K., Bershadsky, M. A., Law, D. R., et al. 2015, ApJ, 798, 7, doi: [10.1088/0004-637X/798/1/7](https://doi.org/10.1088/0004-637X/798/1/7)
- Burstein, D. 1982, ApJ, 253, 539, doi: [10.1086/159656](https://doi.org/10.1086/159656)
- Carr et al., A. in prep.
- Chaussidon, E., Yèche, C., Palanque-Delabrouille, N., et al. 2023, ApJ, 944, 107, doi: [10.3847/1538-4357/acb3c2](https://doi.org/10.3847/1538-4357/acb3c2)
- Cooper, A. P., Kposov, S. E., Allende Prieto, C., et al. 2023, ApJ, 947, 37, doi: [10.3847/1538-4357/acb3c0](https://doi.org/10.3847/1538-4357/acb3c0)
- Cover, T., & Hart, P. 1967, IEEE Transactions on Information Theory, 13, 21, doi: [10.1109/TIT.1967.1053964](https://doi.org/10.1109/TIT.1967.1053964)
- Davis, T. M., & Scrimgeour, M. I. 2014, MNRAS, 442, 1117, doi: [10.1093/mnras/stu920](https://doi.org/10.1093/mnras/stu920)
- DESI Collaboration, Aghamousa, A., Aguilar, J., et al. 2016a, arXiv e-prints, arXiv:1611.00036, <https://arxiv.org/abs/1611.00036>
- DESI Collaboration, Aghamousa, A., Aguilar, J., et al. 2016b, arXiv e-prints, arXiv:1611.00037, doi: [10.48550/arXiv.1611.00037](https://doi.org/10.48550/arXiv.1611.00037)
- DESI Collaboration, Abareschi, B., Aguilar, J., et al. 2022, AJ, 164, 207, doi: [10.3847/1538-3881/ac882b](https://doi.org/10.3847/1538-3881/ac882b)
- DESI Collaboration, Abdul-Karim, M., Adame, A. G., et al. 2025, arXiv e-prints, arXiv:2503.14745, doi: [10.48550/arXiv.2503.14745](https://doi.org/10.48550/arXiv.2503.14745)

- Dey, A., Schlegel, D. J., Lang, D., et al. 2019, *AJ*, 157, 168, doi: [10.3847/1538-3881/ab089d](https://doi.org/10.3847/1538-3881/ab089d)
- Djorgovski, S., & Davis, M. 1987, *ApJ*, 313, 59, doi: [10.1086/164948](https://doi.org/10.1086/164948)
- Douglass, K., BenZvi, S., Ueroi, N., et al. 2025, *arXiv e-prints*, arXiv:2507.11765, doi: [10.48550/arXiv.2507.11765](https://doi.org/10.48550/arXiv.2507.11765)
- Dressler, A., Lynden-Bell, D., Burstein, D., et al. 1987, *ApJ*, 313, 42, doi: [10.1086/164947](https://doi.org/10.1086/164947)
- Flaugher, B., Diehl, H. T., Honscheid, K., et al. 2015, *AJ*, 150, 150, doi: [10.1088/0004-6256/150/5/150](https://doi.org/10.1088/0004-6256/150/5/150)
- Foreman-Mackey, D. 2016, *The Journal of Open Source Software*, 1, 24, doi: [10.21105/joss.00024](https://doi.org/10.21105/joss.00024)
- Guy, J., Bailey, S., Kremin, A., et al. 2023, *AJ*, 165, 144, doi: [10.3847/1538-3881/acb212](https://doi.org/10.3847/1538-3881/acb212)
- Hahn, C., Wilson, M. J., Ruiz-Macias, O., et al. 2023, *AJ*, 165, 253, doi: [10.3847/1538-3881/accff8](https://doi.org/10.3847/1538-3881/accff8)
- Harris, C. R., Millman, K. J., van der Walt, S. J., et al. 2020, *Nature*, 585, 357, doi: [10.1038/s41586-020-2649-2](https://doi.org/10.1038/s41586-020-2649-2)
- Harrison, E. R. 1974, *ApJL*, 191, L51, doi: [10.1086/181545](https://doi.org/10.1086/181545)
- Haynes, M. P., Giovanelli, R., Kent, B. R., et al. 2018, *ApJ*, 861, 49, doi: [10.3847/1538-4357/aac956](https://doi.org/10.3847/1538-4357/aac956)
- Hubble, E. 1929, *Proceedings of the National Academy of Science*, 15, 168, doi: [10.1073/pnas.15.3.168](https://doi.org/10.1073/pnas.15.3.168)
- Hunter, J. D. 2007, *Computing in Science & Engineering*, 9, 90, doi: [10.1109/MCSE.2007.55](https://doi.org/10.1109/MCSE.2007.55)
- Kourkchi, E., Tully, R. B., Anand, G. S., et al. 2020a, *ApJ*, 896, 3, doi: [10.3847/1538-4357/ab901c](https://doi.org/10.3847/1538-4357/ab901c)
- Kourkchi, E., Tully, R. B., Eftekharzadeh, S., et al. 2020b, *ApJ*, 902, 145, doi: [10.3847/1538-4357/abb66b](https://doi.org/10.3847/1538-4357/abb66b)
- Lai et al., Y. in prep.
- Levi, M., Bebek, C., Beers, T., et al. 2013, *arXiv e-prints*, arXiv:1308.0847, doi: [10.48550/arXiv.1308.0847](https://doi.org/10.48550/arXiv.1308.0847)
- Makarov, D., Prugniel, P., Terekhova, N., Courtois, H., & Vauglin, I. 2014, *A&A*, 570, A13, doi: [10.1051/0004-6361/201423496](https://doi.org/10.1051/0004-6361/201423496)
- Masters, K. L., Springob, C. M., Haynes, M. P., & Giovanelli, R. 2006, *ApJ*, 653, 861, doi: [10.1086/508924](https://doi.org/10.1086/508924)
- McInnes, L., Healy, J., & Melville, J. 2018, *arXiv preprint arXiv:1802.03426*. <https://arxiv.org/abs/1802.03426>
- Miller, T. N., Doel, P., Gutierrez, G., et al. 2024, *AJ*, 168, 95, doi: [10.3847/1538-3881/ad45fe](https://doi.org/10.3847/1538-3881/ad45fe)
- Milvang-Jensen, B., Aragón-Salamanca, A., Hau, G. K. T., Jørgensen, I., & Hjorth, J. 2003, *MNRAS*, 339, L1, doi: [10.1046/j.1365-8711.2003.06324.x](https://doi.org/10.1046/j.1365-8711.2003.06324.x)
- Mocz, P., Green, A., Malacari, M., & Glazebrook, K. 2012, *MNRAS*, 425, 296, doi: [10.1111/j.1365-2966.2012.21458.x](https://doi.org/10.1111/j.1365-2966.2012.21458.x)
- Mould, J. 2020, *Frontiers in Astronomy and Space Sciences*, 7, 21, doi: [10.3389/fspas.2020.00021](https://doi.org/10.3389/fspas.2020.00021)
- Moustakas, J., Lang, D., Dey, A., et al. 2023, *ApJS*, 269, 3, doi: [10.3847/1538-4365/acfaa2](https://doi.org/10.3847/1538-4365/acfaa2)
- Myers, A. D., Moustakas, J., Bailey, S., et al. 2023, *AJ*, 165, 50, doi: [10.3847/1538-3881/aca5f9](https://doi.org/10.3847/1538-3881/aca5f9)
- Nakamura, O., Aragón-Salamanca, A., Milvang-Jensen, B., et al. 2006, *MNRAS*, 366, 144, doi: [10.1111/j.1365-2966.2005.09834.x](https://doi.org/10.1111/j.1365-2966.2005.09834.x)
- Phillips, M. M. 1993, *ApJL*, 413, L105, doi: [10.1086/186970](https://doi.org/10.1086/186970)
- Pierce, M. J., & Tully, R. B. 1988, *ApJ*, 330, 579, doi: [10.1086/166495](https://doi.org/10.1086/166495)
- Ponomareva, A. A., Verheijen, M. A. W., Peletier, R. F., & Bosma, A. 2017, *MNRAS*, 469, 2387, doi: [10.1093/mnras/stx1018](https://doi.org/10.1093/mnras/stx1018)
- Poppett, C., Tyas, L., Aguilar, J., et al. 2024, *AJ*, 168, 245, doi: [10.3847/1538-3881/ad76a4](https://doi.org/10.3847/1538-3881/ad76a4)
- Qin et al., F. in prep.
- Raichoor, A., Moustakas, J., Newman, J. A., et al. 2023, *AJ*, 165, 126, doi: [10.3847/1538-3881/acb213](https://doi.org/10.3847/1538-3881/acb213)
- Ravi, N., Douglass, K. A., & Demina, R. 2023, *arXiv e-prints*, arXiv:2310.11422, doi: [10.48550/arXiv.2310.11422](https://doi.org/10.48550/arXiv.2310.11422)
- Riess, A. G., Yuan, W., Macri, L. M., et al. 2022, *ApJL*, 934, L7, doi: [10.3847/2041-8213/ac5c5b](https://doi.org/10.3847/2041-8213/ac5c5b)
- Robotham, A. S. G., & Obreschkow, D. 2015, *PASA*, 32, e033, doi: [10.1017/pasa.2015.33](https://doi.org/10.1017/pasa.2015.33)
- Ross, A. J., Aguilar, J., Ahlen, S., et al. 2025, *JCAP*, 2025, 125, doi: [10.1088/1475-7516/2025/01/125](https://doi.org/10.1088/1475-7516/2025/01/125)
- Ross et al., C. in prep.
- Said, K., Howlett, C., Davis, T., et al. 2024, *arXiv e-prints*, arXiv:2408.13842, doi: [10.48550/arXiv.2408.13842](https://doi.org/10.48550/arXiv.2408.13842)
- Sandage, A., & Tammann, G. A. 1976, *ApJ*, 210, 7, doi: [10.1086/154798](https://doi.org/10.1086/154798)
- Saulder, C., Howlett, C., Douglass, K. A., et al. 2023, *MNRAS*, 525, 1106, doi: [10.1093/mnras/stad2200](https://doi.org/10.1093/mnras/stad2200)
- Schlafly, E. F., Kirkby, D., Schlegel, D. J., et al. 2023, *AJ*, 166, 259, doi: [10.3847/1538-3881/ad0832](https://doi.org/10.3847/1538-3881/ad0832)
- Silber, J. H., Fagrelus, P., Fanning, K., et al. 2023, *AJ*, 165, 9, doi: [10.3847/1538-3881/ac9ab1](https://doi.org/10.3847/1538-3881/ac9ab1)
- Smee, S. A., Gunn, J. E., Uomoto, A., et al. 2013, *AJ*, 146, 32, doi: [10.1088/0004-6256/146/2/32](https://doi.org/10.1088/0004-6256/146/2/32)
- Sofue, Y., & Rubin, V. 2001, *ARA&A*, 39, 137, doi: [10.1146/annurev.astro.39.1.137](https://doi.org/10.1146/annurev.astro.39.1.137)
- Stein, G., Harrington, P., Blaum, J., Medan, T., & Lukić, Z. 2021, *arXiv preprint arXiv:2110.13151*. <https://arxiv.org/abs/2110.13151>
- Tonry, J., & Schneider, D. P. 1988, *AJ*, 96, 807, doi: [10.1086/114847](https://doi.org/10.1086/114847)
- Tully, R. B., & Courtois, H. M. 2012, *ApJ*, 749, 78, doi: [10.1088/0004-637X/749/1/78](https://doi.org/10.1088/0004-637X/749/1/78)
- Tully, R. B., & Fisher, J. R. 1977, *A&A*, 54, 661

- Tully, R. B., & Pierce, M. J. 2000, *ApJ*, 533, 744,
doi: [10.1086/308700](https://doi.org/10.1086/308700)
- Turner et al., R. in prep.
- Virtanen, P., Gommers, R., Oliphant, T. E., et al. 2020,
Nature Methods, 17, 261, doi: [10.1038/s41592-019-0686-2](https://doi.org/10.1038/s41592-019-0686-2)
- Zhou, R., Dey, B., Newman, J. A., et al. 2023, *AJ*, 165, 58,
doi: [10.3847/1538-3881/aca5fb](https://doi.org/10.3847/1538-3881/aca5fb)
- Zhou, R., Guy, J., Koposov, S. E., et al. 2024, arXiv
e-prints, arXiv:2409.05140,
doi: [10.48550/arXiv.2409.05140](https://doi.org/10.48550/arXiv.2409.05140)
- Ziegler, B. L., Böhm, A., Jäger, K., Heidt, J., & Möllenhoff,
C. 2003, *ApJL*, 598, L87, doi: [10.1086/379623](https://doi.org/10.1086/379623)
- Zou, H., Zhou, X., Fan, X., et al. 2017, *PASP*, 129, 064101,
doi: [10.1088/1538-3873/aa65ba](https://doi.org/10.1088/1538-3873/aa65ba)